$\beta - Na_{1.7}IrO_3$: a tridimensional Na-Ion insertion material with a redox active oxygen network

β-$Na_{1.7}IrO_3$: a tridimensional Na-ion insertion material with a redox active oxygen network

P.E. Pearce[1,2,3], G. Rousse[1,2,3], O.M. Karakulina[4], J. Hadermann[4], G. Van Tendeloo[4], D. Foix[5], François Fauth[6], A.M. Abakumov[7] and J.M. Tarascon[1,2,3]

[1] Collège de France, Chimie du Solide et de l'Energie - UMR CNRS 8260, 11 Place Marcelin Berthelot, 75005 Paris, France
[2] Réseau sur le Stockage Electrochimique de l'Energie (RS2E) - FR CNRS 3459, 80039 Amiens Cedex, France
[3] Sorbonne Universités, UPMC Univ Paris 06, 4 Place Jussieu, 75005 Paris, France
[4] EMAT, University of Antwerp, Groenenborgerlaan 171, B-2020, Antwerp, Belgium
[5] IPREM/ECP (UMR 5254), Université de Pau, 2 Avenue Pierre Angot, 64053 Pau Cedex 9, France
[6] CELLS - ALBA synchrotron, Cerdanyola del Vallès, Barcelona E-08290, Spain
[7] Center for Electrochemical Energy Storage, Skolkovo Institute of Science and Technology, Nobel str. 3, 143026 Moscow, Russia
*Corresponding author: J.-M. Tarascon: jean-marie.tarascon@college-de-france.fr

Abstract: The revival of the Na-ion battery concept has prompted an intense search for new high capacity Na-based positive electrodes. Recently, emphasis has been placed on manipulating Na-based layered compounds to trigger the participation of the anionic network. We further explored this direction and show the feasibility of achieving anionic-redox activity in 3-dimensional Na-based compounds. A new 3D β-$Na_{1.7}IrO_3$ phase was synthesized in a two-step process, which involves first the electrochemical removal of Li from β-Li_2IrO_3 to produce β-IrO_3, which is subsequently reduced by electrochemical Na insertion. We show that β-$Na_{1.7}IrO_3$ can reversibly uptake nearly 1.3 Na^+ per formula unit through an uneven voltage profile characterized by the presence of four plateaus related to structural transitions. Surprisingly, the β-$Na_{1.7}IrO_3$ phase was found to be stable up to 600°C, while it could not be directly synthesized via conventional synthetic methods. Although these Na-based iridate phases are of limited practical interest, they help to understand how introducing highly polarizable *guest* ions (Na^+) into *host* rocksalt-derived oxide structures affects the anionic redox mechanism.

Introduction

Electrochemical energy storage is of paramount importance to the transition from fossil fuels to renewable energy sources[1]. Today's portable electronics and the automotive industry heavily rely on the Li-ion technology because it shows the highest energy density and a good reliability[2]. However, the cost and the limited Li resources have driven research towards alternative battery technologies. Among them, the Na-ion technology was already considered thirty years ago but fell into oblivion because of the incredible soar of the Li-ion batteries[3]. Today this technology is gaining considerable interest for applications for which volume is of less importance.

As Na-ion batteries have lower energy densities than Li-ion batteries, it is imperative to develop new highly performing insertion materials, both for

negative and positive electrodes. The recent discovery of an anionic redox activity in Li-rich layered phases[4,5] leading to staggering capacity increases has prompted the study of Na-rich layered compounds with success. Cumulative cationic and anionic redox processes leading to extra-capacities were first reported during Na extraction in $Na_2Ru_{1-y}Sn_yO_3$ and later in Na_2RuO_3 and Na_2IrO_3.[6–8] These phases, which can be written as $Na[Na_{0.33}M_{0.66}]O_2$, crystallize in the well-known layered rocksalt-type structure, alike their Li-rich counterparts. Within the structure, pure Na layers alternate with NaM_2 layers (M – transition metal or spectator cation) for which the NaO_6 octahedra are all edge-shared with MO_6 octahedra to form a honeycomb pattern. This layered structure is prone to gliding of the oxygen close-packed planes since their stacking can reversibly change from O3 to O1 type as recently observed for Na_2IrO_3 upon removal of 1.5 Na^+.[7,8] The same Na removal limitation was observed for Na_2RuO_3 with an additional complexity associated to the feasibility of preparing an ordered or disordered phase depending on the synthesis conditions.[6]

A similar inability to fully remove the alkali ions from the structure was also experienced for the layered α-Li_2IrO_3 phase.[8] This was circumvented by switching to the 3D polymorph β–Li_2IrO_3 which also exhibits a rocksalt-type close-packed structure.[9] However, the distribution of Li and Ir in the structure generates a tridimensional arrangement of edge-sharing IrO_6 octahedra which is frequently referred to as the "hyperhoneycomb" structure.[10] Along the same line of thinking, we decided to study the sodium isomorph of β-Li_2IrO_3, which is the object of this paper.

We herein describe the feasibility to synthesize a new three-dimensional β-Na_xIrO_3 phase via a low temperature process using β–Li_2IrO_3, prepared via a reproducible and well controlled high temperature route, as a precursor. The new Na-based phase was studied for its structural and electrochemical properties. We show that it can reversibly release 1.3 Na^+ per Ir atom via several phase transitions whose mechanisms are detailed below.

Experimental section

Synthesis

β-$Na_{1.7}IrO_3$ was obtained by a two-step electrochemical process. The first is the total delithiation of β-Li_2IrO_3 to obtain IrO_3. This is done by charging the powder vs Li metal in a Swagelok type cell using 1M lithium hexafluorophosphate ($LiPF_6$) in ethylene carbonate/propylene carbonate/dimethyl carbonate (EC/PC/DMC) in a 1/1/3 ratio as electrolyte and a Whatman GF/D borosilicate glass fiber membrane as electronic separator. The IrO_3 powder is then retrieved and thoroughly washed with DMC and dried under vacuum. The second step is the electrochemical sodiation of IrO_3 to obtain β-$Na_{1.7}IrO_3$. Similarly to the first step, this is done by discharging the IrO_3 powder vs Na metal in a Swagelok type cell using 1M sodium hexafluorophosphate ($NaPF_6$) in PC as electrolyte and the same glass fiber separator as previous step. The powder is then retrieved and thoroughly washed with DMC and dried under vacuum.

Electrochemistry

Electrochemical testing was done in Swagelok or 2032 type coin cells as specified, using $Na_{1.7}IrO_3$ mixed with 10% carbon super P as positive electrode and either Na metal or hard carbon as negative electrode. A Whatman GF/D borosilicate glass fiber membrane soaked with 1M $NaPF_6$ in PC was used as separator and electrolyte. For half cells, 1% fluoroethylene carbonate (FEC) was used as electrolyte additive. The cells were assembled in an Ar-filled glovebox and were cycled at a rate of C/10 (1 li^+ removed in 10h) if not specified otherwise.

X-ray Diffraction

Operando and *ex situ* XRD measurements were performed at ALBA synchrotron's MSPD beamline[11] with a wavelength of 0.41226 Å and in a BRUKER D8 Advance diffractometer with Cu Kα radiation ($\lambda_{K\alpha1}$ = 1.54056 Å, $\lambda_{K\alpha1}$ = 1.54439 Å) using a home designed cell equipped with beryllium windows.[12] For the pristine β-$Na_{1.7}IrO_3$ sample, the XRD pattern was collected at the MSPD beamline using a sealed quartz capillary (prepared in an Ar-filled glovebox) inserted in a 0.3mm Kapton capillary.

X-ray Photoelectron Spectroscopy

XPS measurements were carried out with a Kratos Axis Ultra spectrometer, using focused monochromatic Al Kα radiation (hν = 1486.6 eV). The analyzed area of the samples was 300×700 μm² and peaks were recorded with constant pass energy of 20eV. Under the recording conditions, the Ag $3d_{5/2}$ line appeared at 368.3eV and its full width at half-maximum (FWHM) was 0.58 eV. The pressure in the analysis chamber was around 5×10^{-9} mbar. Short acquisition time spectra were recorded before and after each normal experiment to check that the samples did not suffer from degradation during the measurements. The binding energy scale was calibrated using the C 1s peak at 285.0 eV from the hydrocarbon contamination invariably present. To avoid any error on the calibration choice and for more precision, binding energy difference between the O1s lattice and metal core peaks was also examined. Core peaks were analyzed using a nonlinear Shirley-type background[13]. The peak positions and areas were optimized by a weighted least-squares fitting method using 70% Gaussian, 30% Lorentzian line shapes. Quantification was performed on the basis of Scofield's relative sensitivity factors.[14] The curves fit for core peaks were obtained using a minimum number of components in order to fit the experimental curves. The XPS spectrometer was directly connected through a transfer chamber to an argon dry box in which the samples are handled, in order to avoid moisture/air exposure of the samples.

Scanning Transmission Electron Microscopy

The samples were prepared by dipping a Cu TEM grid covered with a holey carbon layer in the powder. No solvent was used. A Gatan vacuum transfer holder was used to protect the specimen from air. The TEM study was performed at a FEI Titan³ cubed microscope operated at 300 kV.

Results and discussion

Synthesis

Our attempts to synthesize 3D β-Na_2IrO_3 through solid state synthesis by playing on several experimental parameters (annealing and cooling rates, annealing and quenching temperatures as well as modifying the heating atmospheres) were not successful, as we uniquely obtained the layered α-Na_2IrO_3 phase or the oxidized α-$NaIrO_3$ phase. We thus decided to implement our strategy earlier developed for $Na_2Ru_{1-y}Sn_yO_3$; it consists in the delithiation of the lithium counterpart ($Li_2Ru_{1-y}Sn_yO_3$) prior to electrochemical sodiation. Hence, the need to master the preparation of the parent β-Li_2IrO_3 phase through ceramic synthesis which, if not otherwise optimized, can lead to a mixture of α and β polymorphs.

In this context, we identified a new and reproducible protocol requiring two consecutive firing steps to prepare pure β-Li_2IrO_3. It first consists in mixing Li_2CO_3 and Ir metal powders (10% in excess) by hand grinding. The mixture is then inserted into a covered alumina crucible and placed in a muffled furnace. The furnace temperature is raised at 3°C/min to 1080°C and maintained at this temperature for 30 hours prior to cooling by switching the furnace off. The resulting powder is

composed of large glittering black particles whose XRD pattern shows that it is composed of β-Li_2IrO_3 and around 10 % IrO_2, resulting from the excess of Ir in the initial precursor mixture. We note that the β polymorph content in the recovered powders is higher as the size of the particles is larger, hence implying a peculiar nucleation-growth process of this phase.

At this stage, the amount of IrO_2 is assessed by Rietveld refinement (≈10-15 %) and the appropriate amount of Li_2CO_3 is added to the recovered powder. The hand grinded mixture is treated following the same firing sequence as before to obtain pure β-Li_2IrO_3. The pattern can be indexed in the *F d d d* space group with the cell parameters a = 5.90783(7) Å, b = 8.45298(8) Å and c = 17.81094(16) Å. The pattern could be refined according to the Rietveld method as presented in Figure 1 b. Scanning electron microscopy (SEM) images show that the particles are between a few microns and a few tens of microns in size (see Figure 1a). It is worth mentioning that the use of a cover together with the excess of Ir is mandatory during our first synthesis step to rapidly obtain the β phase. Indeed, it allows a higher IrO_3 vapor pressure in the reactor, which enables the ripening of the particles and their growth to sizes above 10 µm.[15] Otherwise, there is first the nucleation of the α-polymorph that eventually transforms to the β-polymorph after lengthy annealing treatments at T> 1000°C.

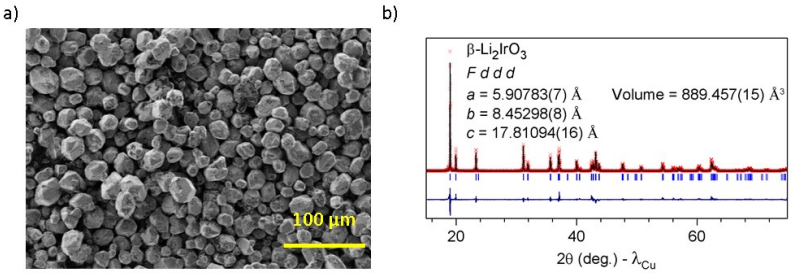

Figure 1 a) Scanning electron microscopy image and b) Rietveld refinement of the X-Ray diffraction pattern of pristine β-Li_2IrO_3. In red are the experimental points, in black is the calculated pattern and in blue the difference between the experimental and calculated patterns. The vertical blue lines beneath the patterns indicate the positions of the Bragg reflections.

The β-Na_xIrO_3 polymorph was then obtained from β-Li_2IrO_3 via electrochemical delithiation followed by resodiation realized at room temperature as follows. Li-half cells using β-Li_2IrO_3 as the positive electrode, 1M $LiPF_6$ in EC:PC:DMC 1:1:3 as electrolyte and a Li metal disk as the negative electrode were first electrochemically charged to 4.6 V to obtain Li-free β-IrO_3 (Figure 2, blue curve). Once recovered and thoroughly washed with DMC, β-IrO_3 was electrochemically discharged versus Na metal in Swagelok cells using 1M $NaPF_6$ in PC as electrolyte solution in view of obtaining "β-Na_xIrO_3".

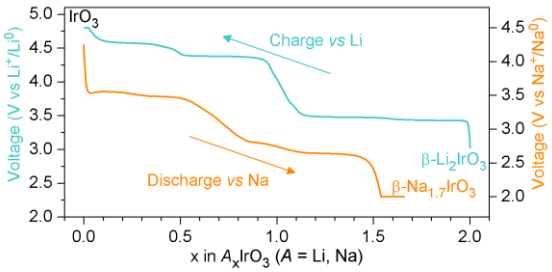

Figure 2 Voltage-composition curves of β-Li_2IrO_3 versus Li metal on charge (blue) between 3.0 V and 4.6 V (versus Li^+/Li^0) and of the subsequent discharge versus Na metal (orange) between 4.2 V and 2.0 V (versus Na^+/Na^0).

The electrochemical discharge profile for the IrO_3/Na cell shown in Figure 2 (orange) resembles the discharge trace collected for a Li/Li_2IrO_3 cell. Indeed, four distinct plateaus can be observed and

the amount of alkali that can be inserted after full charge is similar (1.7 Na^+ vs 1.8 Li^+). Moreover, the voltage trace for the Na cell is, as expected, shifted towards lower potentials because of the lower reducing potential of $Na_{(s)}/Na^+_{(aq)}$ (-2.72 V vs NHE) vs. that of $Li_{(s)}/Li^+_{(aq)}$ (-3.05 V vs NHE). Lastly, we found that no extra Na^+ can be inserted in $Na_{1.7}IrO_3$ by lowering the potential window to 1 V, in contrast to Li_2IrO_3 which can uptake 0.5 Li^+ ($Li_{2.5}IrO_3$) upon reduction to 1.5 V. Structural hindrance linked to the greater size of Na^+ as compared to Li^+ is most likely at the origin of this difference. Note that the potential of the $Na_{1.7}IrO_3$ phase is lower than the stability window of H_2O indicating the sensitivity of this phase to moisture. In line of this observation we observe that $Na_{1.7}IrO_3$ loses Na when left for a few hours in ambient atmosphere.

Structural Characterization

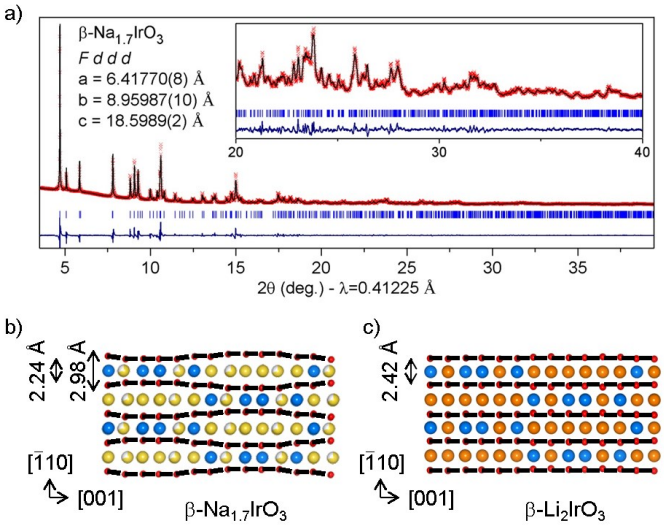

Figure 3 a) Rietveld refinement of synchrotron data of β-$Na_{1.7}IrO_3$ with an enlargement of the 20°-40° region as inset and the extracted cell parameters (observed pattern in red, calculated pattern in black, difference between the observed and calculated patterns in dark blue and the Bragg reflections as blue ticks). b) Structure of β-$Na_{1.7}IrO_3$ and c) of β-Li_2IrO_3. The black dotted lines highlight the oxygen sublattice and the distances between subsequent oxygen layers are given on the left of each figure. Ir, O, Na and Li are in blue, red, yellow and orange respectively.

The powder diffraction pattern for the β-$Na_{1.7}IrO_3$ phase collected on the Materials Science and Powder Diffraction Beamline (MSPD) at ALBA synchrotron with a wavelength of 0.41226 Å was refined using the Rietveld method (Figure 3). All the peaks could be indexed using the same orthorhombic unit cell with *F d d d* space group as the pristine lithiated compound, however with increased cell parameters: a = 6.41770(8) Å, b = 8.95987(10) Å, c = 18.5989(2) Å for $Na_{1.7}IrO_3$ versus a = 5.90783(7) Å, b = 8.45298(8) Å, c = 17.81094(16) Å for Li_2IrO_3. This corresponds to a large cell expansion compared to the Li counterpart (+ 20% in volume). The structure of $Na_{1.7}IrO_3$ was then refined according to the Rietveld method, starting from the structural model of β-Li_2IrO_3 and replacing Li with Na. The Na content was initially fixed to 1.7 per formula unit and the XRD pattern did not evidence any feature that would support some Na/vacancy ordering. However, our refinements indicated that vacancies are located on the Na2 site only, while the Na1 site is fully occupied. The final structural parameters are given in Table 1 and the resulting refinement is shown in Figure 3a.

Table 1 Crystallographic data and atomic positions of β-$Na_{1.7}IrO_3$ determined by Rietveld refinement of synchrotron X-ray powder diffraction pattern.

Atom	Wyckoff position	x/*a*	y/*b*	z/*c*	Occupancy	B (Å²)
Ir1	16*g*	1/8	1/8	0.70875(15)	1	0.61(3)
Na1	16*g*	1/8	1/8	0.0426(13)	1	0.58(12)
Na2	16*g*	1/8	1/8	0.8834(12)	0.7	0.58(12)
O1	16*e*	0.833(3)	1/8	1/8	1	0.33(14)
O2	32*h*	0.644(3)	0.3521(9)	0.0358(6)	1	0.33(14)

Space group *F d d d*. *a* = 6.41767(8) Å; *b* = 8.95985(10) Å; *c* = 18.5988(2) Å; *V* = 1069.45(2) Å^3; R_{Bragg} = 2.94 %; χ^2 = 6.904.

The model obtained from the Rietveld refinement shows strongly distorted oxygen rows along the [001] direction. Indeed, the O2 atom is shifted from the position it occupies in the Li compound. As a result, the oxygen rows running parallel to [001] are considerably displaced outwards, away from each other when they surround Na, while they get closer when they cross Ir (Figure 3b). These corrugated oxygen rows can also be observed by high resolution annular bright field scanning transmission electron microscopy (ABF-STEM) when viewing along the [110] direction (Figure 4 a). A simulation of the ABF-STEM image nicely confirms this observation (Figure 4 b). It is worth mentioning that such corrugated oxygen rows were also reported for β-Na_2PtO_3 as well as for the high-Tc Bi-based cuprates; the latter were explained in terms of structural strains originating from the mismatch between the two consecutive Bi-O2 and Sr-O layers.[16–18] We believe that the apparent "waviness" of the O layers in $Na_{1.7}IrO_3$ is also caused by a geometrical mismatch between the Na-O and the Ir-O distances. Na^+ being larger than Li^+, the size of the tunnels pertaining to β-$Na_{1.7}IrO_3$ must be also larger than in β-Li_2IrO_3. If we estimate the tunnel size as an average distance between the O layers, we get ~2.61 Å for $Na_{1.7}IrO_3$ and 2.42 Å for β-Li_2IrO_3. Although greater, such enlargement is not sufficient at the center of the tunnels where the O waves move apart, since the local interlayer distance increases to ~2.98 Å (Figure 3 bFigure 4). However, increasing the O interlayer separation is limited by the Ir-O distances in the Ir_2O_{10} dimers of the edge-sharing octahedral units going across the layers. As a result, the "normal" Na-O distances are achieved only for Na1 in the center of the tunnels, whereas Na2 at the sides of the tunnels appears over-bonded (BVS = 1.45), thus the $Na_{1.7}IrO_3$ structure seems to be quite strained. This deformation is also reflected in larger spread of the O-Ir-O octahedral angles in β-$Na_{1.7}IrO_3$ (80.6 – 96.1 deg.) compared to that in β-Li_2IrO_3 (85.4 – 92.2 deg.). The strain, associated with the Na2 position, might be at the origin of its fractional occupancy, experimentally observed in the Rietveld refinement.

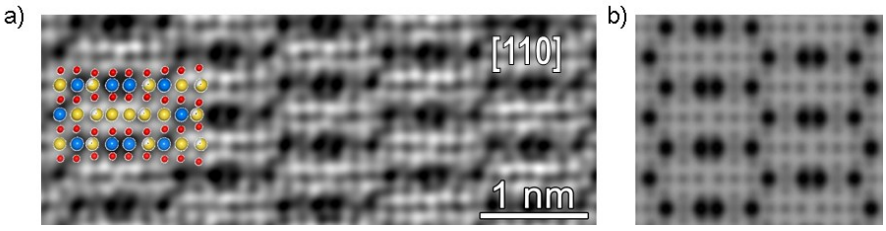

Figure 4 a) Atomic resolution ABF-STEM image of a β-$Na_{1.7}IrO_3$ crystal with corresponding atoms (Ir in blue, O in red and Na in yellow) showing the characteristic view

of the hyperhoneycomb structure along the [110] axis, highlighting the oxygen sublattice distortion. A low bandpass filter was applied. b) ABF-STEM simulation of the β-$Na_{1.7}IrO_3$ structure made using QSTEM software.[19]

***Operando* XRD**

To grasp further insights into the structural changes associated to the insertion and de-insertion of Na into IrO_3, *operando* XRD data were further collected at ALBA synchrotron's MSPD beamline using a home designed cell.[12] IrO_3 was first obtained by electrochemical delithiation of β-Li_2IrO_3 as explained above. The *operando* cell was assembled using IrO_3 mixed with 10% carbon SP and Na metal as the positive and negative electrodes, respectively. The electrodes were electronically separated by a borosilicate glass fiber separator soaked with 1M $NaClO_4$ EC:DMC 1:1 / 1% FEC. This electrolyte composition was tested prior to the experiment and displayed no significant difference on the first cycles. The cell was cycled between 2.0 V and 4.0 V in galvanostatic mode at a C/10 rate with a constant voltage step at the end of discharge and subsequent charge to ensure that a maximum amount of Na^+ is inserted and extracted. Powder XRD patterns were collected with 0.02 steps in the sodium stoichiometry and are shown in Figure 5a.

When discharging the Na/IrO_3 cell we initially observed, through the first plateau process occurring at 3.6 V, a gradual fade of the peaks corresponding to monoclinic IrO_3 (red pattern) at the expense of a new set of peaks which appears and becomes pure for x = 0.5 ($Na_{0.5}IrO_3$, blue pattern). This new phase can be indexed with an orthorhombic unit cell (space group *F d d d)* with the following parameters *a* = 6.9248(6) Å, *b* = 7.7977(9) Å, *c* = 18.0967(10) Å. Upon further insertion through the 3.25 V plateau, the peaks corresponding to the $Na_{0.5}IrO_3$ phase progressively vanish, at the expense of new ones, which give a well-defined XRD pattern for the $Na_{0.75}IrO_3$ composition (green pattern). This phase can also be fully indexed in the *F d d d* orthorhombic cell with *a* = 6.5675(7) Å, *b* = 8.7794(8) Å and *c* = 17.9948(12) Å.

The XRD patterns collected while pursuing the discharge to 2 V clearly evidence the appearance of two new phases of compositions $Na_{1.2}IrO_3$ and $Na_{1.5}IrO_3$ (pink and purple patterns) which form at the end of the 2.5 and 2.2 V plateaus, respectively. Their corresponding lattice cell parameters are *a* = 6.5608(3) Å, *b* = 8.9064(2) Å, *c* = 18.0915(4) Å and *a* = 6.4552(2) Å, *b* = 8.95732(19) Å, *c* = 18.4376(5) Å. Switching to a constant voltage step on discharge when the potential reaches 2 V enables the insertion of 0.2 additional Na^+, hence indicating the poor kinetic of the low voltage Na insertion process. The pattern after this 5 hours process ($Na_{1.7}IrO_3$ in orange) presents slightly different lattice parameters and sharpened peaks (*a* = 6.43960(19) Å, *b* = 8.96034(16) Å and *c* = 18.4999(4) Å).

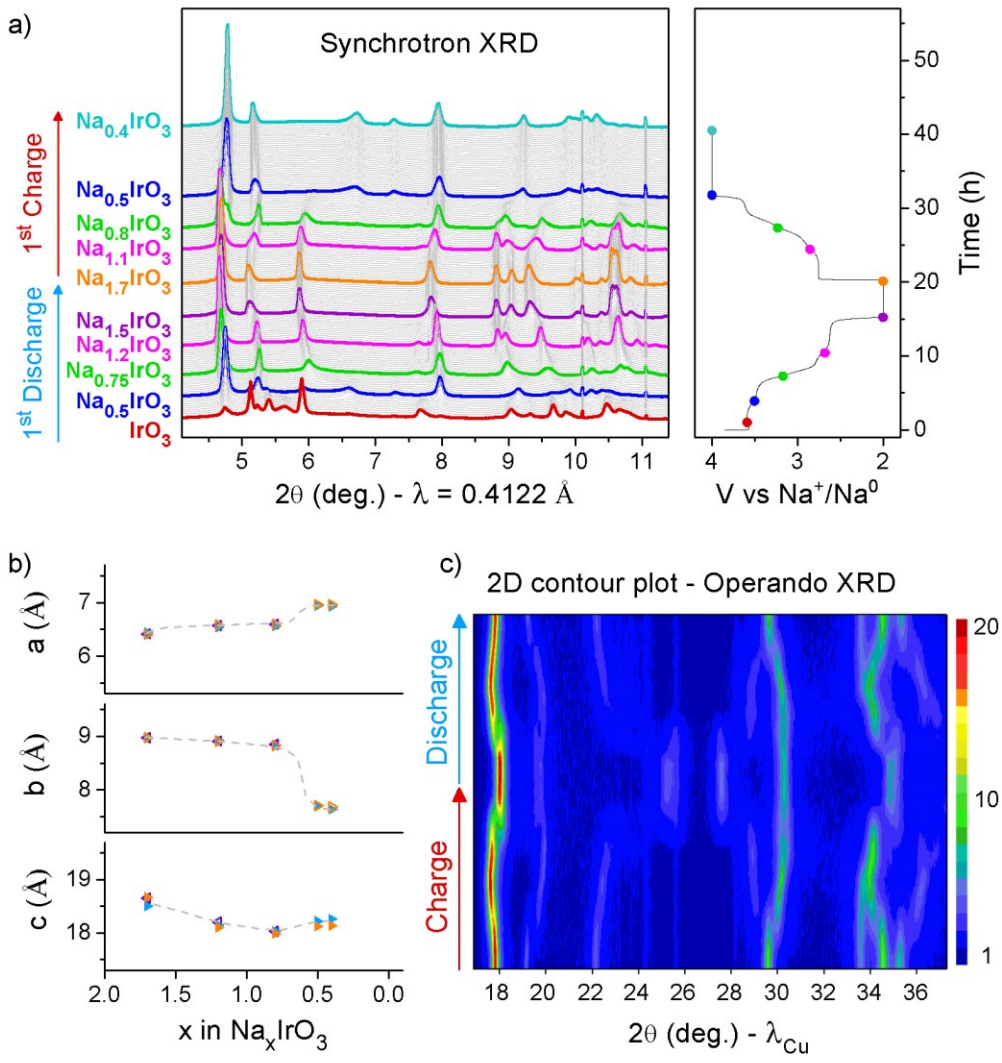

Figure 5 a) Synchrotron *operando* XRD patterns of β-IrO_3 charged vs Na^+/Na^0 and subsequent charge together with the corresponding charge profile. The markers on the charge profile indicate the points where intermediate phases were isolated and the XRD data were refined. Compositions of pure compounds are indicated on the left of the figure. b) Cell parameters obtained by Rietveld refinement of the different intermediate phases during charge and discharge. In blue and orange are the phases during the 1st charge for two different cells and in purple are the phases during subsequent discharge. c) 2D contour plot of lab source *operando* XRD patterns of β-$Na_{1.7}IrO_3$ charged and discharged vs Na^+/Na^0.

On the subsequent charge (Figure 5a), all these processes are reversible with the same sequential appearance of the Na_xIrO_3 phases with the exception that the charged composition is then limited to $Na_{0.4}IrO_3$ even if a constant voltage is applied at 4.0 V. The evolution of the lattice parameters and unit cell volumes during the whole process are reported in Figures 5b and 6, respectively. The unit cell volume monotonously increases with the Na content, from 844 Å^3 for IrO_3 to 1067 Å^3 for $Na_{1.7}IrO_3$ (+26%), and till 977 Å^3 for the following charge ($Na_{0.4}IrO_3$). Such 26% volume increase as compared to solely 5% for the Li system (844 to ~889 Å^3) further stresses the extraordinary flexibility of the IrO_6 scaffold. An *operando* lab XRD experiment on first charge and subsequent discharge of $Na_{1.7}IrO_3$ confirms that these processes are reversible as shown in Figure 5c.

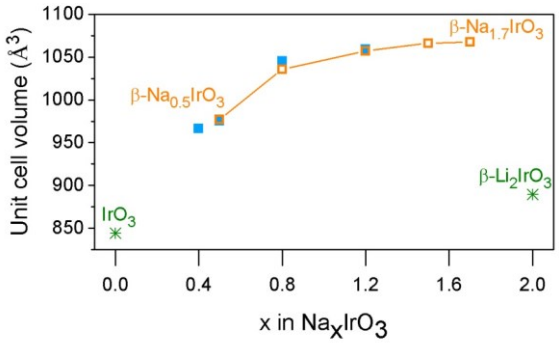

Figure 6 Orthorhombic cell volume of β-Na_xIrO_3 extracted from XRD data using the Rietveld method for different Na content. In orange is the initial discharge from IrO_3, in blue the subsequent charge and in green the orthorhombic equivalent volume of IrO_3 and β-Li_2IrO_3 cell volume for reference.

To better understand the structural changes associated with the Na extraction/insertion, each synchrotron pattern corresponding to single phase intermediate compounds were refined according to the Rietveld method (Supplementary information Figure S1). Our refinements along with atomic resolution high angular annular dark field STEM (HAADF-STEM, collection angles 46-215 mrad) indicate that the IrO_3 scaffold remains intact after insertion of 1.7 Na^+ (Figure 7). However, there is a contraction of the IrO_6 octahedra when the Na content is decreased, which is consistent with the oxidation of Ir^{4+} upon charging.

Moreover, our refinements with different models for Na extraction and insertion (preferential extraction/insertion on Na1 or Na2, or a simultaneous extraction/insertion on both crystallographic sites) show that Na2 is preferentially emptied for Na content between x = 2 and x = 1 (Figure 7). This does not come as a surprise since Na2 is the more constrained Na in the pristine structure. Further desodiation leads to an emptying of the remaining Na1, which is accompanied by a shift in the Na1 position. Interestingly, this shift in position leads to a change of coordination from octahedral to tetrahedral. The bond valence analysis on Na indicates that despite such an unusual coordination for Na, the average Na-O bond length in NaO_4 is 2.30 Å, in agreement with a bond valence sum of 1. However, for the β-$Na_{0.4}IrO_3$ compound, the pattern exhibits pretty broad and asymmetric peak profiles so that the positions of the 0.4 remaining Na atoms are difficult to determine with certainty.

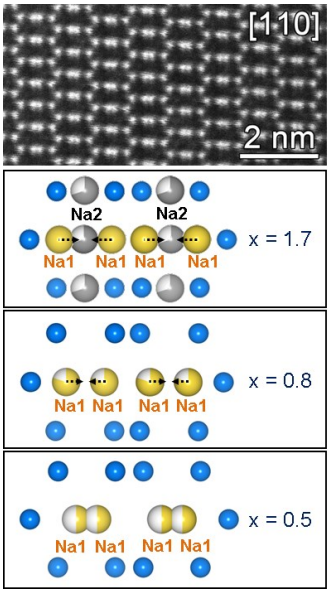

Figure 7. From top to bottom: Atomic resolution HAADF-STEM image of a $Na_{1.7}IrO_3$ particle seen along the [110] direction. Evolution of the Na sites occupation during charge ($Na_{1.7}IrO_3$ to $Na_{0.5}IrO_3$). Ir atoms are represented in blue, Na1 position in yellow and Na2 position in grey.

In order to investigate the charge compensation mechanism within the β-Na_xIrO_3 system, *ex situ* XPS measurements were performed on β-Li_2IrO_3, β-IrO_3, β-$Na_{1.7}IrO_3$ ("Pristine") and β-$Na_{0.4}IrO_3$ (fully charged) samples with a special attention to the Ir 4f and O 1s core spectra. Their binding energy evolution is shown in Figure 8. The evolution of the binding energies of the Ir 4f core peaks clearly indicates a reduction of Ir on discharge from IrO_3 to β-$Na_{1.7}IrO_3$ and an oxidation on charge to β-$Na_{0.4}IrO_3$. The shift towards lower binding energy observed between β-Li_2IrO_3 and β-$Na_{1.7}IrO_3$ is most likely due to the different environment (Na^+ vs Li^+) rather than a

lower oxidation state. Turning to the O 1s binding energy, there is the emergence of a new peak at ~531 eV in going from β-Li_2IrO_3 → β-IrO_3 previously associated to the formation of peroxo-like $(O_2)^{n-}$ anionic species. The intensity of this peak is noted to largely decrease upon reinsertion of Na^+ into β-IrO_3, but its disappearance is not complete for the composition β-$Na_{1.7}IrO_3$. We note a regain in intensity of this peak upon removal of Na as shown for the composition β-$Na_{0.4}IrO_3$ (Fig. 8b bottom). Altogether, this clearly indicates that the anionic redox process involving $(O_2)^{n-}$ species in addition to the reversible cationic activity of Ir is an integral part of the charge compensation mechanism.

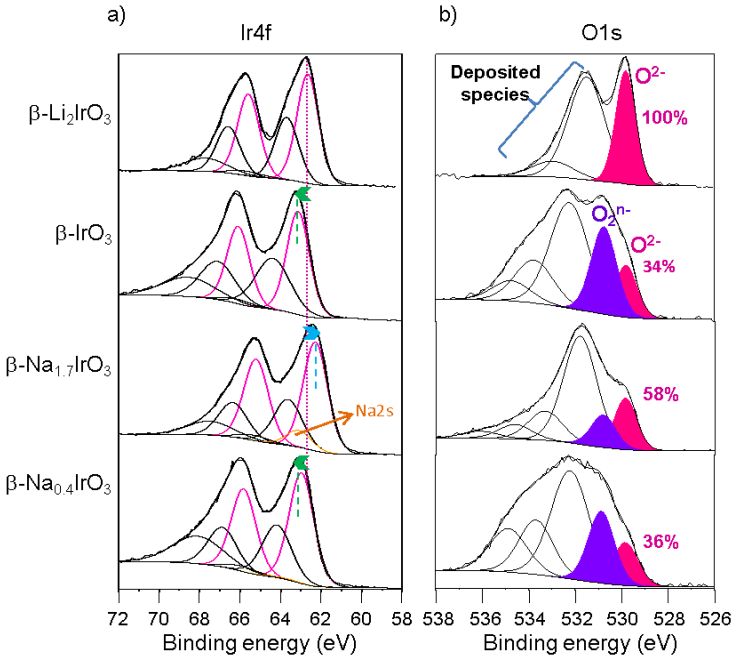

Figure 8. Ir *4f* (a) and O *1s* (b) XPS core spectra collected *ex situ* for β-Li_2IrO_3 IrO_3, β-$Na_{1.7}IrO_3$ and β-$Na_{0.4}IrO_3$.

Electrochemical behavior

To investigate the long-term cycling stability of this new compound, half cells composed of IrO_3 mixed with 10% carbon super P as cathodes and Na metal as anodes using 1M $NaPF_6$ in PC with 1% FEC as electrolyte additive were cycled at a rate of C/10 (1 Na in 10 h). We found a rapid capacity decay upon cycling (Figure 9 a, b) which can be rooted in either a loss of electronic percolation within the electrode due the electrochemical grinding effect upon cycling resulting from repeated volume contraction/expansion or the growth of a blocking SEI resulting from copious electrolyte degradation in the presence of Na as previously reported for layered α-Na_2IrO_3.[8]

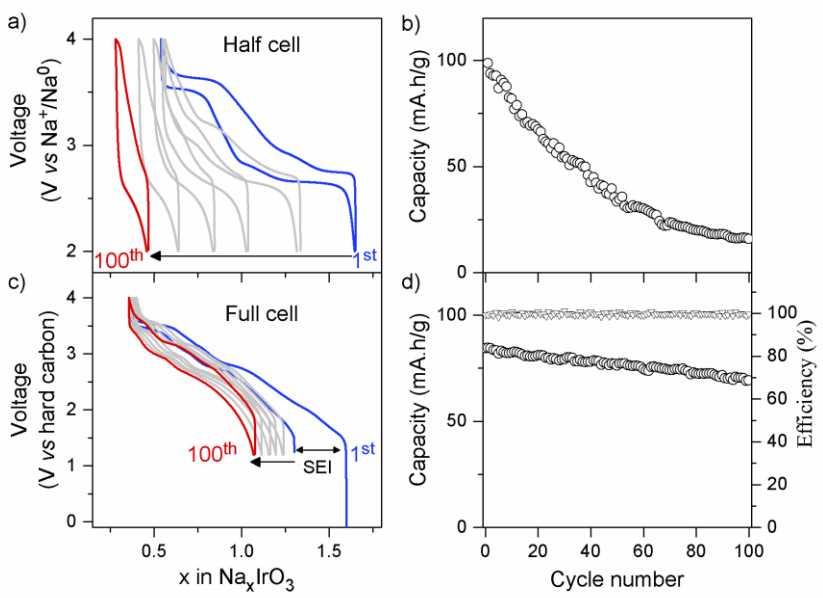

Figure 9 a) The galvanostatic cycling of $Na_{1.7}IrO_3$ in half cell configuration using Na metal as anode and 1M $NaPF_6$ in PC with 1%FEC as electrolyte solution. The 1st cycle is in blue, the 20th, 40th, 60th and 80th cycles are in grey and 100th cycle is in red. b) The capacity retention upon cycling. c) The galvanostatic cycling of $Na_{1.7}IrO_3$ in full cell configuration using hard carbon as anode and 1M $NaPF_6$ in PC as electrolyte solution. The 1st cycle is in blue, the 20th, 40th, 60th and 80th cycles are in grey and 100th cycle is in red. d) The capacity retention (circles) and coulombic efficiency (triangles) upon cycling (first cycle efficiency is 76%)

To decipher between the two possibilities, 2032-type coin cells using β-$Na_{1.7}IrO_3$ mixed with 10% carbon super P as positive electrode, commercial hard carbon as negative electrode and 1M $NaPF_6$ in PC as electrolyte were assembled and cycled at a C/10 rate between 1 and 4 V (Figure 9). The first cycle has a high irreversible capacity due to the formation of an SEI on the hard carbon anode. However, the cell retains up to 82 % of its initial capacity after 100 cycles with a coulombic efficiency of around 99.5 %. This implies that the capacity loss observed in Na half cells was mainly due to electrolyte degradation products from the Na metal anode. However, the greater capacity slippage at the discharge endpoint than at the charge endpoint suggests parasitic reactions occurring at the hard carbon anode. This can explain the slight capacity loss observed.

Thermal stability

Our inability to prepare β-$Na_{1.7}IrO_3$ by solid state synthesis suggests that this phase is thermodynamically less stable than the layered polymorph. To get further insight into the temperature stability issue, differential scanning calorimetry (DSC) measurements were carried-out for both Na_1IrO_3 and $Na_{1.7}IrO_3$. Since these samples (particularly $Na_{1.7}IrO_3$) are moisture sensitive, they were placed in Al pans that were sealed within the dry box. Prior to being placed in the DSC cavity, the pans were quickly pierced while flushing under argon and the measurements collected. After the measurement the Al pan was rapidly returned to the dry-box and the recovered powder was X-rayed using an air-tight cell. Figure 10 shows the XRD patterns of both Na_1IrO_3 and $Na_{1.7}IrO_3$ after the DSC experiment compared to the same composition during *operando* XRD experiment. Both display sharper peaks implying improved crystallinity and negligible peak

shifting after annealing step. In addition, no sign of the layered polymorph could be detected meaning that no phase transition occurred during heating. We therefore conclude that these phases are stable at least to 600°C; the maximum we could measure by DSC experiment.

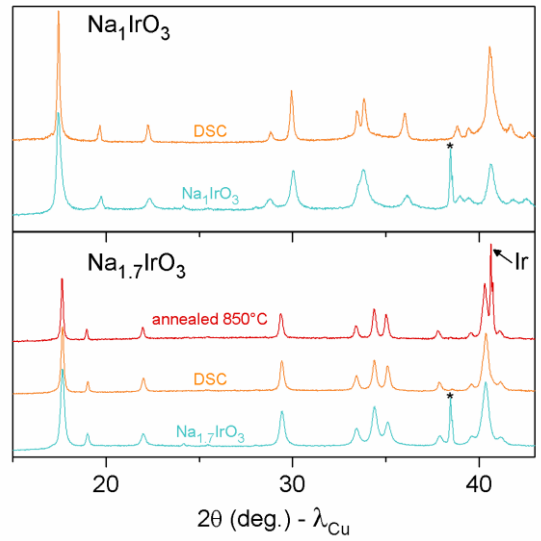

Figure 10 XRD patterns of Na_1IrO_3 and $Na_{1.7}IrO_3$ from in situ measurements (in blue) and after DSC experiment (in orange) and in the case of $Na_{1.7}IrO_3$ the pattern after annealing at 850°C for 6h (in red). Peaks marked by a black star are from the electrochemical cell.

To check the stability towards higher temperatures, $Na_{1.7}IrO_3$ powder was placed in a covered alumina crucible, inserted into an evacuated sealed quartz ampoule and heated to 850°C for 6 hours. After cooling, the ampoule was opened in the dry-box and the powder recovered for XRD characterization. The collected pattern reveals the existence of two distinct phases, with the dominant one Na_xIrO_3 being contaminated by Ir metal (≈ 35% by Rietveld refinement). To assess the Na content (x) of the main phase, the X-ray diffraction data were refined by the Rietveld method. Surprisingly, the obtained cell parameters (a = 6.409(3) Å, b = 8.976(7) Å, c = 18.646(8) Å) only slightly differ from that of the pristine $Na_{1.7}IrO_3$ (a = 6.4068(6) Å, b = 8.9590(11) Å, c = 18.6942(18) Å). This implies that the Na composition slightly deviates from x = 1.7, implying a slow decomposition process from the particle surface inward with surface decomposing yielding volatile Na_2O and Ir metal. This instability toward Na loss is likely to be the main difficulty to overcome in order to prepare β-$Na_{1.7}IrO_3$ via a solid state method.

Using a similar protocol we found that the electrochemically prepared β-Na_1IrO_3 phase is stable up to 550°C while we could not succeed in preparing this phase by solid state reactions from a mixing of Na_2CO_3 and either Ir or IrO_2, suggesting the importance of the precursors (nature and numbers) in controlling the reacting path. We should recall that the free energy of the reaction ΔG decreases by increasing the number of reagents so that it reaches a point at which the reaction will no longer occur (ΔG>0).

Conclusion

We report the room temperature synthesis of a new sodium rich compound with a tridimensional structure β-$Na_{1.7}IrO_3$ within which the oxygen atoms form a waving path. Alike its Li counterpart, it shows an electrochemical activity with the feasibility to reversibly uptake nearly 1.3 Na^+ at an average voltage of 2.4 V with a good capacity retention as deduced by the assembly of full $Na_{1.7}IrO_3$/C Na-ion cells. Moreover, the uptake/release of Na^+ in β-$Na_{1.7}IrO_3$ is shown to occur via several structural phases that differ in terms of lattice parameters while preserving the same IrO_3 framework and with a charge compensation mechanism that reveals the cumulative activity of the cationic (Ir^{5+}/Ir^{4+}) and anionic $(O_2)^{n-}$ networks. Understanding why this phase cannot be straightly synthesized at 1000°C from Ir and alkaline oxides based precursors still remains a puzzle and more so as it remains stable till 700°C once electrochemically prepared and does not transform into the layered Na_xIrO_3. To answer this

question, additional theoretical work aiming to determine the energy landscape of the Na-Ir-O system is being pursued.

Acknowledgements

The authors thank A. Perez for fruitful discussions and his valuable help in synchrotron XRD experiment. This work is based on experiments performed on the Materials Science and Powder Diffraction Beamline at ALBA synchrotron (proposal number 2016091814), Cerdanyola del Vallès, E-08290 Barcelona, Spain. J.-M.T. acknowledges funding from the European Research Council (ERC) (FP/2014)/ERC Grant-Project 670116-ARPEMA. G. R. acknowledges funding from ANR DeliRedox. O. M. K., J. H. and A. M. A. are grateful to FWO Vlaanderen for financial support under grant G040116N.

Supporting information.

Rietveld refinements of Na_xIrO_3 intermediates during charge and discharge, .CIF file of $Na_{1.7}IrO_3$ structure.

References

(1) Larcher, D.; Tarascon, J.-M. Towards Greener and More Sustainable Batteries for Electrical Energy Storage. *Nature Chemistry* **2014**, *7* (1), 19–29.

(2) Etacheri, V.; Marom, R.; Elazari, R.; Salitra, G.; Aurbach, D. Challenges in the Development of Advanced Li-Ion Batteries: A Review. *Energy & Environmental Science* **2011**, *4* (9), 3243–3262.

(3) Yabuuchi, N.; Kubota, K.; Dahbi, M.; Komaba, S. Research Development on Sodium-Ion Batteries. *Chemical Reviews* **2014**, *114* (23), 11636–11682.

(4) Sathiya, M.; Rousse, G.; Ramesha, K.; Laisa, C. P.; Vezin, H.; Sougrati, M. T.; Doublet, M.-L.; Foix, D.; Gonbeau, D.; Walker, W.; Prakash, A. S.; Ben Hassine, M.; Dupont, L.; Tarascon, J.-M. Reversible Anionic Redox Chemistry in High-Capacity Layered-Oxide Electrodes. *Nature Materials* **2013**, *12* (9), 827–835.

(5) McCalla, E.; Abakumov, A. M.; Saubanère, M.; Foix, D.; Berg, E. J.; Rousse, G.; Doublet, M.-L.; Gonbeau, D.; Novák, P.; Van Tendeloo, G.; Dominko, R.; Tarascon, J.-M. Visualization of O-O Peroxo-like Dimers in High-Capacity Layered Oxides for Li-Ion Batteries. *Science* **2015**, *350* (6267), 1516–1521.

(6) Rozier, P.; Sathiya, M.; Paulraj, A.-R.; Foix, D.; Desaunay, T.; Taberna, P.-L.; Simon, P.; Tarascon, J.-M. Anionic Redox Chemistry in Na-Rich Na2Ru1−ySnyO3 Positive Electrode Material for Na-Ion Batteries. *Electrochemistry Communications* **2015**, *53*, 29–32.

(7) Mortemard de Boisse, B.; Liu, G.; Ma, J.; Nishimura, S.; Chung, S.-C.; Kiuchi, H.; Harada, Y.; Kikkawa, J.; Kobayashi, Y.; Okubo, M.; Yamada, A. Intermediate Honeycomb Ordering to Trigger Oxygen Redox Chemistry in Layered Battery Electrode. *Nature Communications* **2016**, *7*, 11397.

(8) Perez, A. J.; Batuk, D.; Saubanère, M.; Rousse, G.; Foix, D.; McCalla, E.; Berg, E. J.; Dugas, R.; H. W. van den Bos, K.; Doublet, M.-L.; Gonbeau, D.; Abakumov, A. M.; Van Tendeloo, G.; Tarascon, J.-M. Strong Oxygen Participation in the Redox Governing the Structural and Electrochemical Properties of Na-Rich Layered Oxide Na_2IrO_3. *Chemistry of Materials* **2016**, *28* (22), 8278–8288.

(9) Pearce, P. E.; Perez, A. J.; Rousse, G.; Saubanère, M.; Batuk, D.; Foix, D.; McCalla, E.; Abakumov, A. M.; Van Tendeloo, G.; Doublet, M.-L.; Tarascon, J.-M. Evidence for Anionic Redox Activity in a Tridimensional-Ordered Li-Rich Positive Electrode β-Li2IrO3. *Nature Materials* **2017**, *16* (5), 580–586.

(10) Biffin, A.; Johnson, R. D.; Choi, S.; Freund, F.; Manni, S.; Bombardi, A.; Manuel, P.; Gegenwart, P.; Coldea, R. Unconventional Magnetic Order on the Hyperhoneycomb Kitaev Lattice in β − Li 2 IrO 3 : Full Solution via Magnetic Resonant X-Ray Diffraction. *Physical Review B* **2014**, *90* (20), 205116.

(11) Fauth, F.; Boer, R.; Gil-Ortiz, F.; Popescu, C.; Vallcorba, O.; Peral, I.; Fullà, D.; Benach, J.; Juanhuix, J. The Crystallography Stations at the Alba Synchrotron. *The European Physical Journal Plus* **2015**, *130* (8), 160.

(12) Leriche, J. B.; Hamelet, S.; Shu, J.; Morcrette, M.; Masquelier, C.; Ouvrard, G.; Zerrouki, M.; Soudan, P.; Belin, S.; Elkaïm, E.; Baudelet, F. An Electrochemical Cell for Operando Study of Lithium Batteries Using Synchrotron Radiation. *Journal of The Electrochemical Society* **2010**, *157* (5), A606–A610.

(13) Shirley, D. A. High-Resolution X-Ray Photoemission Spectrum of the Valence Bands of Gold. *Physical Review B* **1972**, *5* (12), 4709–4714.

(14) Scofield, J. H. Hartree-Slater Subshell Photoionization Cross-Sections at 1254 and 1487 eV. *Journal of Electron Spectroscopy and Related Phenomena* **1976**, *8* (2), 129–137.

(15) Freund, F.; Williams, S. C.; Johnson, R. D.; Coldea, R.; Gegenwart, P.; Jesche, A. Single Crystal Growth from Separated Educts and Its Application to Lithium Transition-Metal Oxides. *Scientific Reports* **2016**, *6* (35362).

(16) Tarascon, J.-M.; Le Page, Y.; Barboux, P.; Bagley, B. G.; Greene, L. H.; McKinnon, W. R.; Hull, G. W.; Giroud, M.; Hwang, D. M. Crystal Substructure and Physical Properties of the Superconducting Phase Bi 4 (S R, C a) 6 Cu 4 O 1 6+ X. *Physical Review B* **1988**, *37* (16), 9382–9389.

(17) Urland, W.; Hoppe, R. Zur Kenntnis Der Oxoplatinate Na2PtO2, Na2PtO3, „K2PtO3" Und „Rb2PtO3". *Zeitschrift für anorganische und allgemeine Chemie* **1972**, *392* (1), 23–36.

(18) Zandbergen, H. W.; Groen, W. A.; Mijlhoff, F. C.; van Tendeloo, G.; Amelinckx, S. Models for the Modulation in A2B2CanCu1+nO6+2n, A, B=Bi, Sr OR Tl, Ba and n=0, 1, 2. *Physica C: Superconductivity* **1988**, *156* (3), 325–354.

(19) Christoph Koch. Determination of Core Structure Periodicity and Point Defect Density along Dislocations. PhD, ARIZONA STATE UNIVERSITY, 2002.